Journal of Environmental Management 398 (2026) 128396

Contents lists available at ScienceDirect

Journal of Environmental Management

journal homepage: www.elsevier.com/locate/jenvman

Research article

Surface-engineered anisotropic Fe_3O_4 nanoplates for highly efficient magnetic field-assisted micro/nanoplastics remediation

Yujeong Jeong [a,1], Eun-Hye Jang [a,1], Gaeun Kim [a], Kyubeom Lee [a], Joonkyung Jang [b], Sungwook Chung [a,c,d,*]

[a] School of Chemical Engineering, Pusan National University, 2 Busandaehak-ro 63beon-gil, Geumjeong-gu, Busan, 46241, Republic of Korea
[b] Department of Nanoenergy Engineering, Pusan National University, 2 Busandaehak-ro 63beon-gil, Geumjeong-gu, Busan, 46241, Republic of Korea
[c] School of Chemical and Biomolecular Engineering, Pusan National University, 2 Busandaehak-ro 63beon-gil, Geumjeong-gu, Busan, 46241, Republic of Korea
[d] Institute of Environment & Energy, Pusan National University, 2 Busandaehak-ro 63beon-gil, Geumjeong-gu, Busan, 46241, Republic of Korea

ARTICLE INFO

Keywords:
Magnetite
Surface-engineered nanoplates
Micro/nanoplastics
Remediation
Electrostatic adsorption
Magnetic-field assisted removal

ABSTRACT

Micro- and nanoplastics (MNPs) are emerging contaminants of global concern, but their efficient removal from aqueous environments poses a critical challenge. This paper reports the development of anisotropic magnetite nanoplates (MNPLs) coated uniformly with SiO_2 to yield MNPL@SiO_2 as highly efficient magnetic nano-harvesters for MNPs. Engineering the SiO_2 surface with aminopropyl (NH_2–), octadecyl (C_{18}–), and phenylethyl (Ph–) groups to tune the electrostatic, hydrophobic, and π–π interactions enabled optimally functionalized MNPL@SiO_2 to show rapid and highly efficient MNPs remediation, with 93.4 %, 92.1 %, and 94.3 % removal efficiencies (REs) for 100 nm, 500 nm, and 1 μm polystyrene (PS) MNPs, within 10 min under magnetic field-assisted conditions. The mechanistic insights were obtained through a systematic evaluation of the MNPs removal kinetics and isotherms. The kinetic data followed a pseudo-second order model, indicating chemi-sorption driven by electrostatic interactions, while equilibrium adsorption isotherms conformed to the Langmuir model with high sorption capacity (~3630.2 mg/g), outperforming many reported nanostructured adsorbents. In addition to classical adsorption, a secondary mechanism—dynamic trapping—was uncovered when plate-like MNPL@SiO_2 aggregated into hierarchical architectures under a magnetic field that physically entrap unadsorbed MNPs within the void spaces. Dynamic trapping contributed significantly to RE enhancement, where an additional 18.2 % removal was shown. Reusability assessments confirmed that NH_2-MNPL@SiO_2 retained promising activity across multiple cycles after solvent cleaning. These findings highlight the synergistic contributions of shape anisotropy, surface engineering, and magnetic field-assisted dynamic trapping in MNPs removal, providing new mechanistic insights and offering a scalable approach for rapid, efficient, and sustainable water remediation applications.

1. Introduction

Microplastics (MPs) and nanoplastics (NPs), also combined as micro/nanoplastics (MNPs), are small plastic particles. The former and latter have diameters of ≤5 mm and <1 μm, respectively. They originate either from the fragmentation of larger plastic waste caused by the extensive use of plastics, driven by their lightweight, low-cost, and versatile properties, or are intentionally manufactured for use in commercial and industrial products such as cleansing foams, shampoos, toothpastes, and paints or secondary microplastics (Pedrero et al., 2024; Perumpully et al., 2023).

MPs are easily dispersed across terrestrial (Hoang et al., 2024), aquatic (Ahmed et al., 2021; Patidar et al., 2024), and atmospheric (Chen et al., 2020) environments because of their tiny size, where they persist owing to their resistance to geochemical or biological degradation (Eerkes-Medrano et al., 2015). For example, Du et al. investigated suspended atmospheric MPs in a coastal urban zone, which was fiber-dominated, and observed microbeads and films in Xiamen, China,

* Corresponding author. School of Chemical Engineering, Pusan National University, 2 Busandaehak-ro 63beon-gil, Geumjeong-gu, Busan, 46241, Republic of Korea.
E-mail address: sungwook.chung@pusan.ac.kr (S. Chung).
[1] These authors contributed equally to this work.

https://doi.org/10.1016/j.jenvman.2025.128396
Received 21 September 2025; Received in revised form 1 December 2025; Accepted 19 December 2025
Available online 24 December 2025

at levels of 0–0.062 items/m^3, with an average of 0.010 ± 0.012 items/m^3 (Du et al., 2024). Sun et al. reported that atmospheric MPs deposition significantly contributes to MPs pollution in urban waters (Sun et al., 2022). Choi et al. observed 664 items/kg of MPs, such as polyethylene (PE) and polypropylene (PP), in agricultural soils in Yeoju, South Korea (Choi et al., 2021). Patidar et al. reported MPs in the pre-monsoon season in water and sediments (water: 8–26 items/L; sediment: 62–354 items/kg) of the Mahanadi River, India (Patidar et al., 2023b). Cozar et al. investigated MPs, which had a concentration of 0–2500 g/km^2 on the sea surface (Cózar et al., 2014). Therefore, the widespread presence of MPs in oceans, rivers, soils, and even drinking water can pose a significant threat to the environment and health. To address this widespread environmental threat, following the 2022 UNEA resolution, global efforts now mandate a legally binding treaty to address plastic pollution by emphasizing the lifecycle management of MPs (de Sousa, 2024).

MNPs possess a range of physicochemical properties that make them persistent, mobile, and environmentally hazardous. MNPs are typically composed of hydrophobic polymers such as polyethylene (PE), polypropylene (PP), polystyrene (PS), and polyethylene terephthalate (PET). This hydrophobicity enables them to absorb and concentrate toxic organic pollutants, such as polycyclic aromatic hydrocarbons (PAHs), polychlorinated biphenyls (PCBs), and pesticides from the surrounding environments via van der Waals forces (Sankar et al., 2023). In addition, depending on the type of plastics and environmental aging processes such as photooxidation and hydrolysis, MNPs can develop surface functional groups, including hydroxyl, carboxyl, or amino moieties, which change surface charge and modulate electrostatic interactions with hazardous ionic pollutants such as heavy metals, dyes, and pharmaceutical residues. Furthermore, the surface area-to-volume ratio of MNPs increases dramatically as plastic particles become smaller, particularly on the nanoscale. This enhances their reactivity and adsorption capacity, enabling them to act as efficient carriers for toxic pollutants, facilitating their transport and interaction with biological systems at the cellular level, and potentially allowing their entry into the food chain, which poses ecological and human health risks (Chen and Lin, 2024; Dong et al., 2020; Hu et al., 2021; Jin et al., 2022; Patidar et al., 2023a).

A range of conventional physical, chemical, biological, and hybrid techniques has been used to remove MPs from aqueous environments. Physical methods such as filtration, coagulation, flocculation, and sedimentation capture or aggregate MPs, with membranes and adsorbents, offer high efficiency but face challenges of fouling or materials costs (Dayal et al., 2024; Mao et al., 2024). Chabi et al. reported that rapid sand filtration effectively removed MPs smaller than 10 μm with 84 %–98 % efficiencies (Chabi et al., 2024). Chemical methods, including advanced oxidation processes and chemical precipitation, can degrade and separate MPs. Falco et al. reported 65.5 % degradation efficiency of 1 μm PS MPs via an electrochemical oxidation process using boron-doped diamond electrodes over 5 h (Falco et al., 2024). Li et al. showed that microbeads with sizes ranging from 1 mm to over 250 μm could be removed with more than 95 % efficiency using polyaluminum chloride, although microbeads in the 10–250 μm range posed a greater challenge (Li et al., 2024). Biological methods, such as biofilm-mediated trapping and enzymatic degradation, provide environmentally friendly options, but are relatively slower and less efficient. Overall, an effective large-scale remediation requires facile and rapid methods capable of removing MPs and submicron NPs with high removal efficiency, operational feasibility, cost-effectiveness, and minimal secondary pollution.

Magnetite (Fe_3O_4), an iron oxide-based mineral with an inverse cubic spinel structure consisting of FeO and Fe_2O_3, contains Fe^{2+} and Fe^{3+} oxidation states (Fidelis et al., 2025). The combination of crystal structure and electronic configuration gives magnetite superior magnetic properties (Mitra et al., 2024), making it a widely utilized material in biomedical fields, including magnetic resonance imaging (MRI) contrast enhancement, targeted drug delivery, and biosensor development, as well as in biomass harvesting, lipid extraction, and water treatment (Fatmawati et al., 2023; Nguyen et al., 2021). For example, Sumathi et al. presented the use of Fe_3O_4 nanoparticles for the sustainable harvesting of astaxanthin-producing microalgae, advancing the efficiency and scalability of industrial biorefinery processes (Sumathi et al., 2025). Bai et al. designed an integrated system combining adsorption, magnetic separation, and sand filtration system using FMCTO@Fe_3O_4 for As(III) removal from drinking water, showing a trade-off between the arsenic removal efficiency and adsorbent utilization rate, highlighting the importance of optimized adsorbent applications in water treatment (Bai et al., 2025). Beyond these conventional applications, recent studies have increasingly focused on surface-engineering of bare magnetite to overcome its inherent limitations, such as oxidation and rapid aggregation. For instance, Mistral et al. synthesized chitosan-coated superparamagnetic Fe_3O_4 nanoparticles that significantly improved magnetic resonance imaging (MRI) contrast, enhanced magnetic hyperthermia efficiency, and optimized drug delivery performance (Mistral et al., 2024). Seo et al. reported downstream integration of microalgae harvesting and cell disruption using cationic surfactant-decorated Fe_3O_4 nanoparticles, demonstrating the versatility of functionalized magnetite in streamlining complex bioprocesses (Seo et al., 2016). Liang et al. demonstrated surface-engineered Fe_3O_4 as a highly sensitive and selective chemosensor for detecting Cd(II) species (Liang et al., 2025).

Magnetic nanoparticles are promising candidates for removing MNPs using external magnetic fields. Heo et al. used spherical magnetic Fe_3O_4 nanoparticles to remove micron-sized PS MPs (Heo et al., 2022). Wang et al. reported spherical Fe_3O_4 nanoparticles functionalized with superhydrophobic long-chain fatty acid for removing 100 nm PS MPs (Wang et al., 2023). Li et al. designed self-driven Fe_3O_4-based microrobots for removing MNPs from aqueous environments (Li et al., 2022). Despite the progress, many magnetic adsorbents made of isotropic spherical magnetic nanoparticles showed a decline in performance after several adsorption/desorption cycles due to incomplete desorption, loss or leaching of surface functional groups, structural degradation, or irreversible fouling (Pervaiz et al., 2025). Also, some magnetic adsorbents showed slower adsorption kinetics, leading to a long contact time to establish equilibrium (Yoon et al., 2014). In addition, spherical iron oxide nanoparticles showed low adsorption capacity for a broad range of pollutants, because their surface chemistry was not tailored to specific contaminants (Phouthavong et al., 2022). Therefore, achieving high removal efficiencies with relatively rapid kinetics and excellent reusability consistently, particularly for nanoscale plastics, remains a significant challenge. In addition, few studies have systematically investigated the effects of anisotropic morphology, interfacial interactions with MNPs, and magnetic field-mediated aggregation on removal processes.

Herein, anisotropic magnetite nanoplate (MNPL) that is thermally transformed from a hematite analog, was prepared and coated with a uniform SiO_2 layer to fabricate MNPL@SiO_2 as a highly efficient MNPs nanoharvester. The MNPL@SiO_2 surface was functionalized with various organic groups, such as octadecyl (C_{18}–), aminopropyl (NH_2–), and phenylethyl (Ph–) groups, to analyze their roles in enhancing the hydrophobic, electrostatic, and π–π interactions with MNPs, respectively. This study assessed the effectiveness of the functionalized MNPL@SiO_2 in removing MNPs from aqueous environments under magnetic field-assisted conditions. Removal efficiencies (REs) of 93.4 %, 92.1 %, and 94.3 % were achieved within 10 min for 100 nm, 500 nm, and 1 μm PS particles as model MNPs, respectively, when optimally functionalized MNPL@SiO_2 were applied in magnetic field-assisted removal processes. Systematic analyses of the removal efficiency, removal kinetics, and adsorption isotherms revealed important information to elucidate the underlying mechanisms of magnetic field-assisted MNPs removal processes using functionalized anisotropic MNPL@SiO_2.

2. Materials and methods

2.1. Materials

Iron (III) nitrate nonahydrate ($Fe(NO_3)_3 \bullet 9H_2O$, >99 %, KANTO, Japan), aluminum sulfate octadecahydrate ($Al_2(SO_4)_3 \bullet 18H_2O$, ≥99 % Aldrich, USA), iron(III) chloride hexahydrate ($FeCl_3 \bullet 6H_2O$, 98 %, Daejung, Korea), tetraethyl orthosilicate (TEOS) (98 %, Acros Organics, Belgium), cetyltrimethyl ammonium bromide (CTAB, 99 %, Daejung, Korea), 3-aminopropyl triethoxysilane (APTES, 99 %, Aldrich, USA), octadecyltriethoxysilane (ODTES, 98 %, Alfa Aesar, USA), 2-phenylethyltrimethoxysilane (PETMS, 97 %, Gelest Inc., USA), sodium acetate (98.5 %, SAMCHUN, Korea), polyethylene glycol 2000 (PEG, Alfa Aesar, USA), triethylamine ($N(CH_2CH_3)_3$, ≥99 % Junsei, Japan), ammonium hydroxide aqueous solution (NH_4OH, 28–30 %, Daejung, Korea), 1N hydrochloric acid (Daejung, Korea), acetic acid (Daejung, Korea), ethylene glycol (99.5 %, SAMCHUN, Korea), diethylene glycol (99 %, Aldrich, USA) and PS particles with sizes of 100 nm, 500 nm and 1 μm (2 wt%, Aldrich, USA) were purchased and used as received. All other chemicals and solvents, including absolute ethanol and acetone, were of analytical ACS reagent grade and used as received.

2.2. Preparation of hematite (α-Fe_2O_3) nanoplate (HNPL)

HNPL was synthesized using the procedure described elsewhere (Jeong et al., 2023).

2.3. Preparation of SiO_2-coated α-Fe_2O_3 nanoplate (HNPL@SiO_2)

The SiO_2 coating on the HNPL surface was prepared using a modified method reported elsewhere (Liu et al., 2014). First, 0.1 g of the as-prepared HNPL was dispersed in a mixture containing 15 mL of deionized water and 52.5 mL of anhydrous ethanol in an ultrasonic bath (WUC-A10H, DAIHAN, Korea; 40 kHz, 160 W) under ultrasonication for 5 min at room temperature. Subsequently, 3 mL of an aqueous ammonium hydroxide solution was added to the solution under ultrasonication for 5 min, followed by the addition of 7.5 mL of an ethanol solution of CTAB (15 g/L) under ultrasonication for 5 min. A 0.2 mL volume of TEOS in 18 mL ethanol was then added under ultrasonication for 30 min. The products were collected by centrifugation, rinsed three times with absolute ethanol and triply distilled water, and dried overnight in an oven at 60 °C.

2.4. Preparation of SiO_2-coated magnetite (Fe_3O_4) nanoplate (MNPL@SiO_2)

Samples of HNPL and HNPL@SiO_2 were annealed thermally in a furnace under continuously flowing H_2/N_2 mixed gas (H_2/N_2 = 10:90 wt %) at 400 °C for 3 h to obtain MNPL and MNPL@SiO_2, respectively.

2.5. Preparation of aminopropyl functionalized MNPL@SiO_2 (NH_2-MNPL@SiO_2), octadecyl functionalized MNPL@SiO_2 (C_{18}-MNPL@SiO_2) and mixed aminopropyl/octadecyl functionalized MNPL@SiO_2 (NH_2/C_{18}-MNPL@SiO_2)

The MNPL@SiO_2 surface was modified with aminopropyl (NH_2–) and octadecyl (C_{18}–) groups was achieved using a modified version of the method reported by Salman, Ali Dawood et al. (Salman et al., 2021). MNPL@SiO_2 (0.125 g) was dispersed in a solution containing 7.5 mL of deionized water and 42.5 mL of ethanol in an ultrasonic bath (WUC-A10H, DAIHAN, Korea; 40 kHz, 160 W) under ultrasonication for 10 min at 60 °C. Subsequently, 0.378 mL of 1N hydrochloric acid and 0.1 mL of 1N acetic acid were added under ultrasonication for 5 min at 60 °C. Subsequently, 0.1 mL of 1N acetic acid and 1.8 mmol of APTES, 0.1 mL of 1N acetic acid and 1.8 mmol of ODTES, and 0.1 mL of 1N acetic acid, 1.8 mmol of APTES, and ODTES were added under ultrasonication for 4 h at 60 °C to form NH_2-MNPL@SiO_2, C_{18}-MNPL@SiO_2, and NH_2/C_{18}-MNPL@SiO_2, respectively. The products were collected using a neodymium magnet (dimension (length × width × height): 50 × 25 × 10 mm) with a magnetic field strength of 4700 ± 100 G, rinsed repeatedly with absolute ethanol and triply distilled water, and dried in a vacuum oven at 60 °C.

2.6. Preparation of phenylethyl functionalized MNPL@SiO_2 (Ph-MNPL@SiO_2) and mixed aminopropyl/phenylethyl functionalized MNPL@SiO_2 (NH_2/Ph-MNPL@SiO_2)

The MNPL@SiO_2 surface was modified with phenylethyl (Ph–) groups using a modified method reported elsewhere (Kang et al., 2016). MNPL@SiO_2 and NH_2-MNPL@SiO_2 (0.0625 g each) were dispersed in a solution containing 6.81 mL of deionized water, 0.75 mL of NH_4OH, and 60 mL of ethanol in an ultrasonic bath (WUC-A10H, DAIHAN, Korea; 40 kHz, 160 W) under ultrasonication for 10 min at 60 °C. Subsequently, 1.8 mmol of PETMS was added under ultrasonication for 6h at 60 °C to form Ph-MNPL@SiO_2 and NH_2/Ph-MNPL@SiO_2, respectively. The products were collected using a neodymium magnet (dimension (length × width × height): 50 × 25 × 10 mm) with a magnetic field strength of 4700 ± 100 G, rinsed repeatedly with absolute ethanol, chloroform, and triply distilled water, and dried in a vacuum oven at 60 °C.

2.7. Preparation of spherical Fe_3O_4 nanoparticles

Spherical Fe_3O_4 nanoparticles were prepared using the method reported by Huang et al. (2016). $FeCl_3 \bullet 6H_2O$ (1.35 g) was dissolved in a mixture of 40 mL of ethylene glycol and diethylene glycol (35:5, v/v %) and stirred vigorously at 600 rpm for 10 min at room temperature. Subsequently, 3.6 g of sodium acetate and 1.0 g of PEG were added to the mixture and stirred vigorously at 600 rpm for 20 min at room temperature. The mixture was then placed into a 75 mL Teflon-lined stainless-steel autoclave, sealed, and heated to 200 °C under autogenic pressure for 20 h. After the autoclaved materials were cooled to room temperature, the products were rinsed several times with absolute ethanol and triply distilled water before drying in a vacuum oven at 60 °C.

2.8. Magnetic field-assisted MNPs removal experiments

PS particles, 100 nm, 500 nm, and 1 μm in size, were removed using functionalized MNPL@SiO_2 under magnetic field-assisted equilibrium batch conditions. MNPs solutions at predetermined concentrations were made by diluting stock solutions 100 nm, 500 nm, and 1 μm PS particles as model MNPs. All experiments were conducted in duplicate at 25 °C. Briefly, premade MNPs solutions were added to individual 10 mL glass vials containing different amounts of functionalized MNPL@SiO_2 and diluted to obtain a 5 mL solution with final concentrations of 50 mg/L MNPs and 500 mg/L functionalized MNPL@SiO_2. The samples were either in an ultrasonic bath (WUC-A10H, DAIHAN, Korea; 40 kHz, 160 W) under ultrasonication for 10 min or stirred at 500 rpm for 10 min at room temperature to agitate and establish the equilibrium of the suspension. The suspension was then placed under an external magnetic field using a neodymium magnet (dimension (length × width × height): 50 × 25 × 10 mm) with a magnetic field strength of 4700 ± 100 G for 5 min to collect MNPs-functionalized MNPL@SiO_2 adducts. The remaining solutions were analyzed spectrophotometrically using a JP/UV-3600 UV–VIS spectrometer (Shimadzu, Kyoto, Japan) at λ = 247 nm, quantifying the remaining PS particles in the solution in order to assess the MNPs removal. The RE was calculated using the following equation (1), where C_0 and C_f represent the absorbance of the suspension before and after magnetic collection/removal of MNPs, respectively:

$$\text{Removal efficiency (RE) (\%)} = \frac{C_0 - C_f}{C_0} \times 100 \quad (1)$$

The effects of different functionalized MNPL@SiO_2 dosages, agitation times either by sonication or magnetic stirring, pHs, and temperatures were investigated in the range of 100–1000 mg/L, 30 s–30 min, and pH 4.0–10.0, and 20–50 °C, respectively, with a series of MNPs concentrations. The optimal values of dosage, pH, and agitation time for yielding the maximum RE for the remaining experiments were determined.

The effects of the external magnetic field, generated by a neodymium magnet, were evaluated by comparing the REs obtained in the presence and absence of the applied field. Premade MNPs solutions were added to individual 10 mL glass vials containing different amounts of functionalized MNPL@SiO_2 and diluted to obtain a 5 mL solution with final concentrations of 50 mg/L MNPs and 500 mg/L functionalized MNPL@SiO_2. The samples were either placed in an ultrasonic bath (WUC-A10H, DAIHAN, Korea; 40 kHz, 160 W) under ultrasonication for 10 min or stirred at 500 rpm for 10 min at room temperature to agitate and establish the equilibrium of the suspension. The suspension was then placed under an external magnetic field using a neodymium magnet (dimension (length × width × height): 50 × 25 × 10 mm) with a magnetic field strength of 4700 ± 100 G for 5 min to collect MNPs-functionalized MNPL@SiO_2 adducts. For the control experiments, the suspension was subjected to gravitational settling in the absence of an external magnetic field. After complete precipitation of the adducts, the supernatant was analyzed spectrophotometrically using a JP/UV-3600 UV–VIS spectrometer (Shimadzu, Kyoto, Japan) at $\lambda = 247$ nm to determine the removal of MNPs by quantifying the amounts of residual PS particles in the solution.

For the recycling experiments, functionalized MNPL@SiO_2 adsorbents were separated from the suspension and washed twice with 5 mL of the designated solvent, such as water, ethanol, or acetone, under ultrasonic agitation for 5 min. They were then separated using a neodymium magnet, rinsed with deionized water, and dried at 60 °C prior to reuse.

2.9. Analysis of the removal kinetics and adsorption isotherms

One of the major removal mechanisms of MNPs using functionalized MNPL@SiO_2 is adsorption. Pseudo-first-order and pseudo-second-order kinetic models are frequently used to explain the adsorption-based processes. Pseudo-first-order kinetics are based on the assumption that the rate of adsorption is proportional to the number of unoccupied sites on the adsorbent surface. The rate equation is expressed as

$$\frac{dq_t}{dt} = k_1(q_e - q_t)\cdots \tag{2}$$

where t, k_1, q_t, and q_e are the contact time (min), the pseudo-first-order rate constant (min^{-1}), the amount of adsorbed (i.e., the adsorption capacity ($mg{\cdot}g^{-1}$)) at time t, and the adsorption capacity ($mg{\cdot}g^{-1}$) at equilibrium, respectively. The linearized form for fitting the data was derived using the following equation:

$$\ln(q_e - q_t) = \ln(q_e) - k_1 t \tag{3}$$

Pseudo-second-order kinetics are based on the assumption that the rate of adsorption depends on the square of the number of unoccupied sites on the adsorbent surface. The rate equation is expressed as

$$\frac{dq_t}{dt} = k_2(q_e - q_t)^2 \tag{4}$$

where k_2 is the pseudo-second-order rate constant (g/(mg·min)). The linearized form for fitting the data was derived using the following equation:

$$\frac{t}{q_t} = \frac{t}{q_e} + \frac{1}{k_2 q_e^2} \tag{5}$$

The best fits to the removal kinetics data were obtained by linear regression using Eqs. (3) and (5), respectively.

Langmuir, Freundlich, and Temkin models are the three classical adsorption isotherm models used to describe how the adsorbates interact with adsorbent surfaces. The Langmuir model assumes monolayer adsorption on a homogeneous surface where all adsorption sites are identical and energetically equivalent. Once a site is occupied, no further adsorption occurs at that site, with no surface migration of the adsorbed molecules (Foo and Hameed, 2010). The Langmuir isotherm is expressed in the following nonlinear (6) and linearized (7) forms:

$$q = \frac{q_m K_L C_e}{1 + K_L C_e} \tag{6}$$

$$\frac{C_e}{q_e} = \frac{1}{q_m} C_e + \frac{1}{q_m K_L} \tag{7}$$

where q_m, q_e, C_e, and K_L are the maximum adsorption capacity ($mg{\cdot}g^{-1}$), the adsorption capacity at equilibrium ($mg{\cdot}g^{-1}$), the equilibrium concentration of adsorbate ($mg{\cdot}L^{-1}$), and the Langmuir equilibrium constant ($L{\cdot}mg^{-1}$), respectively, related to the binding affinity of the adsorbates. The Freundlich model assumes that adsorption occurs on a heterogeneous surface with sites of different affinities. It describes non-ideal and reversible adsorption that is not limited to monolayer formation. The Freundlich isotherm is expressed in the following nonlinear (8) and linearized (9) forms:

$$q_e = K_F C_e^{\frac{1}{n_F}} \tag{8}$$

$$\log q_e = \log K_F + \frac{1}{n_F} \log C_e \tag{9}$$

where K_F is the Freundlich adsorption constant, and $1/n_F$ is the adsorption intensity, i.e., a measure of surface heterogeneity. The adsorption process is considered favorable if $1/n_F$ is between 0.1 and 1, with larger values indicating weaker adsorption but greater desorption and reusability. The Temkin model accounts for the effects of adsorbate–adsorbate interactions, assuming that the adsorption enthalpy decreases linearly as the surface coverage increases. The Temkin isotherm was expressed in the following nonlinear (10) and linearized (11) forms:

$$q_m = \frac{RT}{b_T} \ln(A_T C_e) \tag{10}$$

$$q_m = \frac{RT}{b_T} \ln C_e + \frac{RT}{b_T} \ln A_T \tag{11}$$

where R, T, A_T, and b_T are the gas constant (i.e., 8.314 J mol^{-1} K^{-1}), the absolute temperature (K), the Temkin isotherm equilibrium binding constant ($L{\cdot}g^{-1}$), and the Temkin isotherm constant related to the heat of adsorption ($J{\cdot}mol^{-1}$), respectively. The linearized form of the three models was used to obtain best fits to the MNPs adsorption equilibrium isotherm data of functionalized MNPL@SiO_2.

2.10. Nanoplate packing simulations

The random packing of circular nanoplates with a fixed thickness of 25 nm was simulated to evaluate the effect of particle size and aspect ratio on packing behavior. The radius of the nanoplates was varied from 350 to 200 nm, and the aspect ratio was defined as the ratio of radius to thickness. Each nanoplate was represented by a discrete cubic grid point spaced 25 nm apart within a cubic box with a side length six times the radius of the nanoplate. A nanoplate was initially placed at the center of the box, and additional nanoplates were placed sequentially. The centers of the new nanoplates were chosen randomly from available grid points, and their orientations were randomized by selecting the axis and angle of rotation, with transformations applied using the appropriate rotation matrix. The processes continued until the box could no longer accommodate additional nanoplates. The packing ratio, defined as the fraction

of grid points occupied by nanoplates relative to the total number of grid points in the simulation box, was calculated. Random placements and movements were implemented using random number generators.

2.11. Statistical analysis

The experimental results are represented as the means ± standard deviation of three independent experiments. Origin Pro software (OriginLab, USA) and Microsoft Office Excel 2016 (Microsoft, USA) were used for the data analysis. A student *t*-test was conducted using Origin Pro, and P values < 0.05 ($^*P < 0.05$) were considered statistically significant.

3. Results and discussion

3.1. Characterization of SiO_2-coated MNPL (MNPL@SiO_2) and derivatization of the SiO_2 surface with aminopropyl, octadecyl, and phenyl functional groups

A previous study reported a method of preparing MNPL having a two-dimensional anisotropic plate-like morphology thermally transformed from HNPL (Jeong et al., 2023). Fig. 1 shows representative FESEM and inset TEM images of HNPL, HNPL@SiO_2, and MNPL@SiO_2. The SiO_2 coating enhanced dispersion, prevented agglomeration, and enabled surface engineering of MNPL with various functional groups, as shown in Scheme 1. Thermal conversion of HNPL to MNPL resulted in minimal morphological changes, as indicated by their structural similarity, as verified by a comparison of the average LSs and TNs of HNPL and MNPL based on an analysis of FESEM, TEM, and AFM measurements (Fig. 1 and S1). In contrast, the mean TN of MNPL increased from 6.8 ± 1.7 to 25.4 ± 6.1 nm when the amorphous SiO_2 layer was grown on the MNPL surface to form MNPL@SiO_2 (Fig. S1). In addition, the *d*-spacing values of HNPL and MNPL, determined from TEM (Fig. 1A–C) and XRD (Fig. 1D) measurements to investigate their crystallinity, agreed with those of nanostructured crystalline hematite (Jeong et al., 2025; Pan et al., 2024) and magnetite (Jing et al., 2025; Liang et al., 2025), respectively.

Fig. 2A shows the FT-IR spectra of MNPL@SiO_2 and functionalized MNPL@SiO_2 with NH_2-MNPL@SiO_2, C_{18}-MNPL@SiO_2, Ph-MNPL@SiO_2, NH_2/C_{18}-MNPL@SiO_2, and NH_2/Ph-MNPL@SiO_2 functional groups. All spectra exhibited common peaks between 561 and 552 cm^{-1}, which were attributed to the Fe–O collective vibrations present in the domain of magnetite (Jeong et al., 2023). In addition, all spectra had IR bands at ~1048 cm^{-1} that were assigned to the antisymmetric stretching Si–O–Si vibration in disordered SiO_2, consistent with values previously reported for silica-based nanomaterials (Shi et al., 2022). The weak IR bands at 1470 and 1552 cm^{-1} observed only from aminopropyl functionalized MNPL@SiO_2, such as NH_2-MNPL@SiO_2, NH_2/C_{18}-MNPL@SiO_2, and NH_2/Ph-MNPL@SiO_2, were assigned to the N–H bending modes of the amino groups from bound APTES (Majoul et al., 2015). The IR bands at 2850 and 2920 cm^{-1} observed only from octadecyl functionalized MNPL@SiO_2, such as C_{18}-MNPL@SiO_2 and NH_2/C_{18}-MNPL@SiO_2, were attributed to the C–H stretching modes of the octadecyl chain from bound ODTES (Kumari et al., 2015; Majoul et al., 2015). The IR bands at 1454 and 1495 cm^{-1} observed only in the phenyl functionalized MNPL@SiO_2, such as Ph-MNPL@SiO_2 and NH_2/Ph-MNPL@SiO_2, were assigned to the characteristic aromatic C=C vibrations from bound PETMS (Asemani and Rabbani, 2020).

Fig. 2B shows survey XPS spectra of functionalized MNPL@SiO_2 over the whole energy range, confirming the presence of Fe, Si, O, N, and C elements. Their high-resolution XPS scans of functionalized MNPL@SiO_2 were analyzed by fitting the XPS data to Lorentzian–Gaussian functions (Fig. S2–6). The resulting binding energies (BEs) of Fe 2p, Si 2p, O 1s, N 1s, and C 1s electrons present in functionalized MNPL@SiO_2 were obtained, as listed in Tables S1–2. A few aspects of the results are worth addressing. First, high-resolution Fe 2p XPS scans of all the functionalized MNPL@SiO_2 showed two asymmetric peaks assigned to Fe $2p_{1/2}$ and $2p_{3/2}$ orbitals (Jeong et al., 2023; Li et al., 2021). The peaks were deconvoluted to identify the chemical states of Fe, differentiating between Fe^{2+} and Fe^{3+}. The former peak was composed of contributions from Fe^{2+} at 722.6–724.8 eV and from Fe^{3+} at 724.0–725.3 eV, while the latter was composed of contributions from Fe^{2+} at 709.8–710.9 eV and from Fe^{3+} at 710.6–713.1 eV, respectively. The calculated Fe^{2+}:Fe^{3+} ratio of 1:2.15, based on the mean relative XPS peak areas, closely matched the stoichiometric 0.33:0.67 ratio of bulk

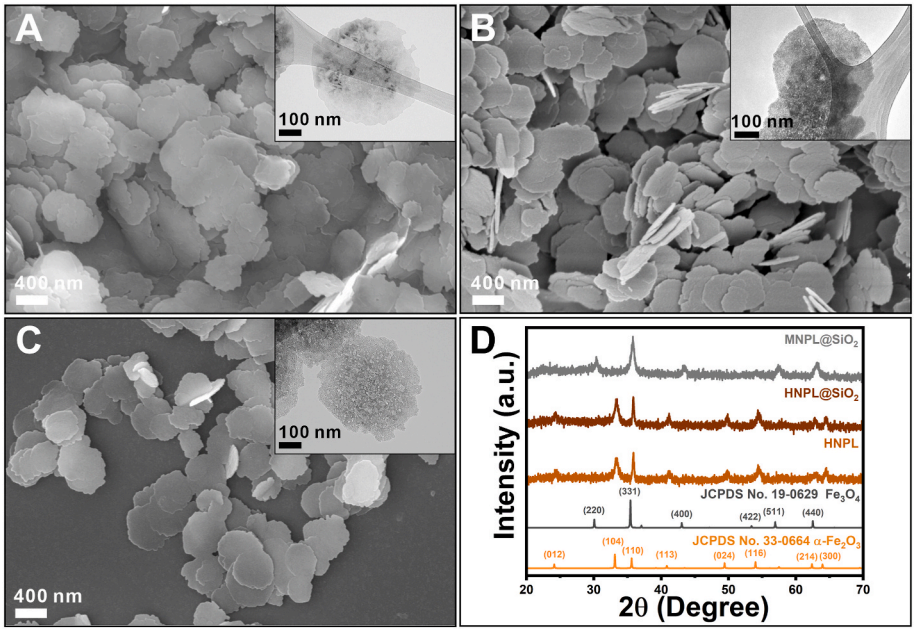

Fig. 1. Representative FESEM images of (A) as-prepared HNPL, (B) HNPL@SiO_2, and (C) MNPL@SiO_2. The inset presents TEM images of single (A) HNPL, (B) HNPL@SiO_2, and (C) MNPL@SiO_2, which show the amorphous SiO_2 layer grown on the surface of HNPL and MNPL. (D) Powder XRD patterns of HNPL, HNPL@SiO_2, and MNPL@SiO_2. The individual peaks were indexed to the appropriate planes of crystalline α-Fe_2O_3 (JCPDS No. 33–0664) and Fe_3O_4 (JCPDS No. 19–0629).

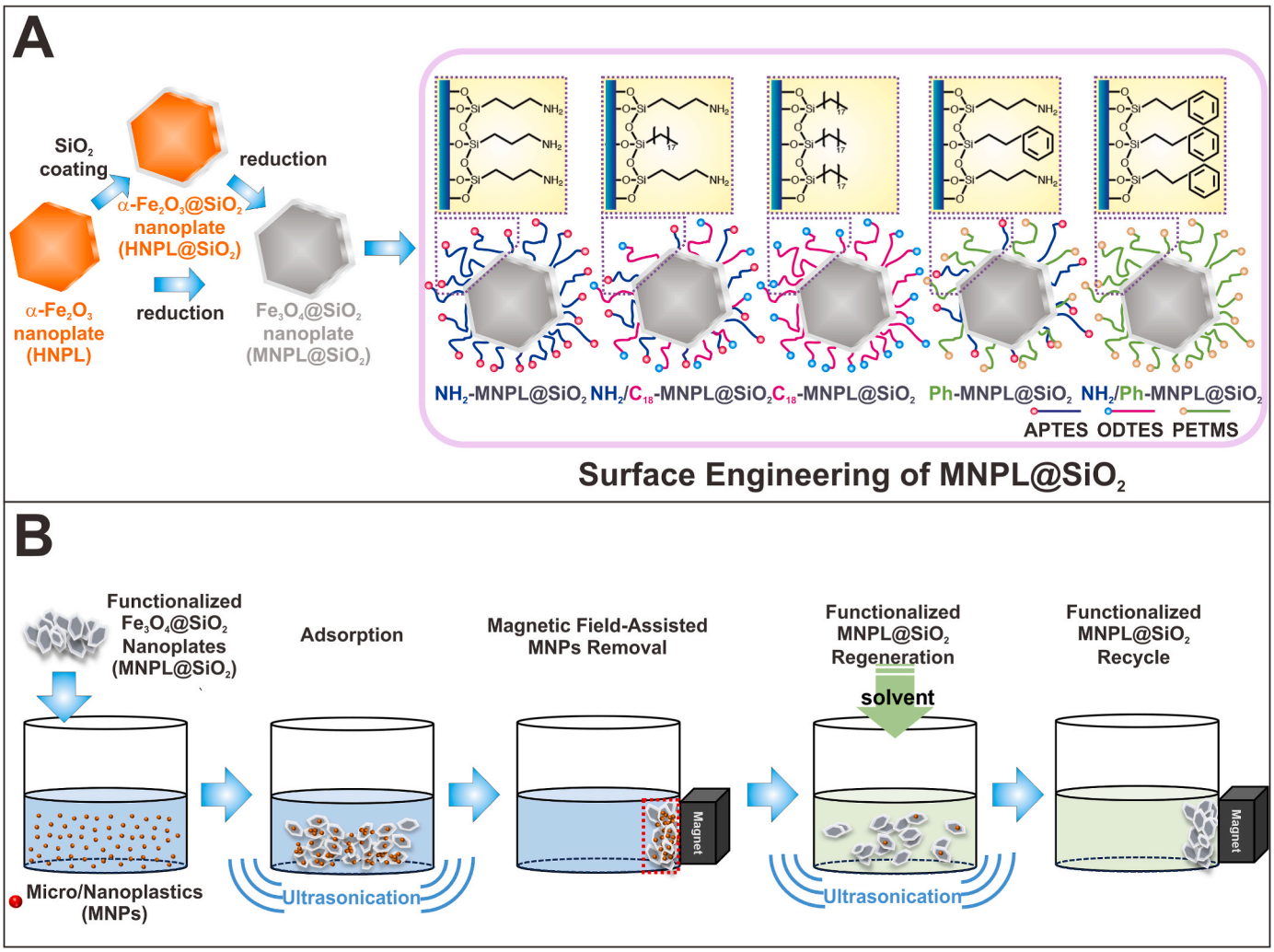

Scheme 1. Schematic diagram of (A) the preparation, surface engineering of SiO_2-coated MNPL (MNPL@SiO_2) from HNPL precursor, and (B) their applications for magnetic field-assisted MNPs removal processes.

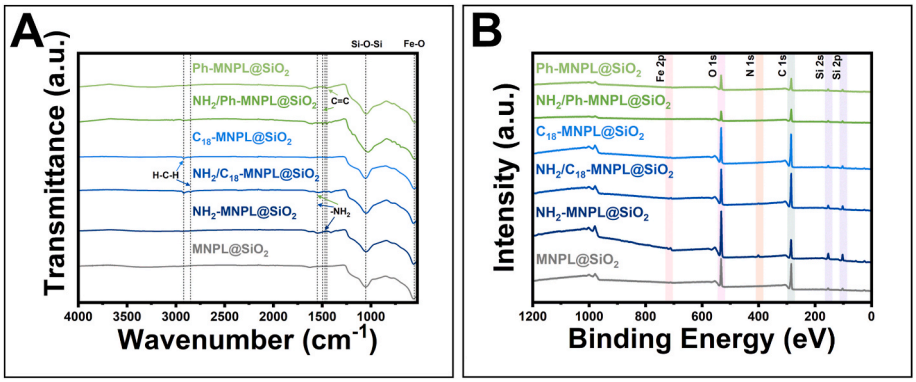

Fig. 2. (A) FT-IR and (B) survey XPS spectra of MNPL@SiO_2, NH_2-MNPL@SiO_2, NH_2/C_{18}-MNPL@SiO_2, C_{18}-MNPL@SiO_2, NH_2/Ph-MNPL@SiO_2, and Ph-MNPL@SiO_2. The dotted lines (FT-IR) and colored regions (XPS) indicate the characteristic IR bands of specific vibrational modes and the characteristic BEs of the elements present in bare and functionalized MNPL@SiO_2, respectively.

magnetite ($Fe(II)O•Fe(III)_2O_3$), with an inverse spinel structure (Huang et al., 2019; Jeong et al., 2023). Second, the deconvolution of the Si 2p spectra from all the functionalized MNPL@SiO_2 revealed a set of four peaks located at ~101.3, ~102.3, ~103.3, and ~104.8 eV regardless of surface functionalization. These BEs were assigned to Si–C, Si–O–Fe, Si–O–Si, and Si–O–C/Si–O, respectively (Chen et al., 2023; Jeong et al., 2025). Third, the deconvolutions of O 1s, N 1s, and C 1s from all the functionalized MNPL@SiO_2 showed slight variations of the BEs because of their characteristic surface functionalization (Fig. S4–6, Table S2). Nevertheless, some of the observed features reflect the characteristic signatures of specific surface functionalization. Fig. S5 shows the deconvoluted N 1s XPS spectra of MNPL@SiO_2 functionalized with

aminopropyl groups, such as NH_2-MNPL@SiO_2, NH_2/C_{18}-MNPL@SiO_2, and NH_2/Ph-MNPL@SiO_2. They were composed of two peaks located at ~399.1 and ~401.4 eV, which were assigned to neutral amino (–NH_2) and cationic ammonium (–NH_3^+) moieties, respectively (Tomić et al., 2021). In addition, the peak at ~286.0 eV in the deconvoluted C 1s XPS spectra (Fig. S6) was assigned to the C–N moieties from MNPL@SiO_2 functionalized with aminopropyl groups.

The amounts of octadecyl, aminopropyl, and phenylethyl groups were estimated by thermogravimetric analysis/differential thermal analysis (TGA/DTA). Fig. 3A presents TGA/DTA curves of functionalized MNPL@SiO_2, illustrating the weight loss profiles as a function of temperature. The aminopropyl group loading value of NH_2-MNPL@SiO_2, NH_2/C_{18}-MNPL@SiO_2, and NH_2/Ph-MNPL@SiO_2 was determined to be ~0.508 mmol g^{-1}. The octadecyl group loading values were for C_{18}-MNPL@SiO_2 and NH_2/C_{18}-MNPL@SiO_2 were ~0.149 mmol g^{-1} and ~0.113 mmol g^{-1}, respectively. Ph-MNPL@SiO_2 and NH_2/Ph-MNPL@SiO_2 exhibited the phenylethyl group loading values of ~0.623 and ~0.487 mmol g^{-1}, respectively. Note that MNPL@SiO_2 bearing mixed functional groups showed smaller loadings than those with single functional groups. The reduced loadings of the octadecyl and phenylethyl groups in mixed-functionalized MNPL@SiO_2 likely result from competition for limited surface silanol sites and steric hindrance between co-functionalized groups, leading to less efficient packing and lower surface coverage. These factors prevent either group from achieving the same surface density as when functionalized alone, resulting in an overall lower functional group loading in the mixed systems.

Fig. 3B shows low-temperature N_2 adsorption–desorption isotherms and pore size distributions of functionalized MNPL@SiO_2. The shapes of all isotherms were similar to that of the characteristic type IV described in the IUPAC classification (Sing, 1985). The hysteresis loops of all isotherms were similar to type H1 hysteresis (IUPAC classification), which is commonly observed in disordered porous silica with cylindrical pores within the same pressure (P/P_0) range (Sing, 1985; Thommes et al., 2015). The specific surface area (S_{BET}) and pore size (d_{pore}) of the bare and functionalized MNPL@SiO_2 were determined from their low-temperature N_2 adsorption–desorption isotherms using the BET and BJH models. Table S3 lists the results. The S_{BET} and d_{pore} of unfunctionalized MNPL@SiO_2 were 186.6 m^2 g^{-1} and 1.10 nm, respectively, because of the SiO_2 layer formed on the MNPL surface. The specific surface areas (SSAs) of functionalized MNPL@SiO_2 were slightly lower than those of the unfunctionalized samples, likely due to the attachment of functional groups on the disordered porous SiO_2 surface (Abdelsamad et al., 2025).

Fig. 3C presents zeta (ζ) potential measurements of bare and functionalized MNPL@SiO_2 as a function of pH. Table S4 lists their zeta potentials. Bare MNPL@SiO_2 exhibited all negative zeta potential values regardless of pH, suggesting that the SiO_2-coated surface of MNPL was negatively charged. The zeta potential values of aminopropyl functionalized MNPL@SiO_2, such as NH_2-MNPL@SiO_2, NH_2/C_{18}-MNPL@SiO_2, and NH_2/Ph-MNPL@SiO_2, remained positive at pH $\leq$ 9 because NH_2–groups (pKa = ~9–10) were protonated under these conditions. On the other hand, they became negative with increasing pH because the amount of deprotonated NH_3^+–groups likely increased.

The contact angles of the unfunctionalized MNPL@SiO_2 and NH_2-MNPL@SiO_2 were 13.3° and 19.6°, respectively (Fig. S7). The contact angles for the octadecyl functionalized MNPL@SiO_2, such as C_{18}-MNPL@SiO_2 and NH_2/C_{18}-MNPL@SiO_2, were 31.7° and 32.5°, respectively, showing a moderate increase compared to the unfunctionalized MNPL@SiO_2 and NH_2-MNPL@SiO_2, likely due to the hydrophobic octadecyl chains. Notably, the contact angles for the phenylethyl functionalized MNPL@SiO_2, such as Ph-MNPL@SiO_2 and NH_2/Ph-MNPL@SiO_2, were 80.6° and 85.6°, respectively, with an increase approximately four times greater than that observed for C_{18}-functionalized MNPL@SiO_2, likely because of the highly hydrophobic phenylethyl groups.

Fig. 3D presents magnetic hysteresis (M–H) curves of bare and functionalized MNPL@SiO_2 that have a similar shape with M_r

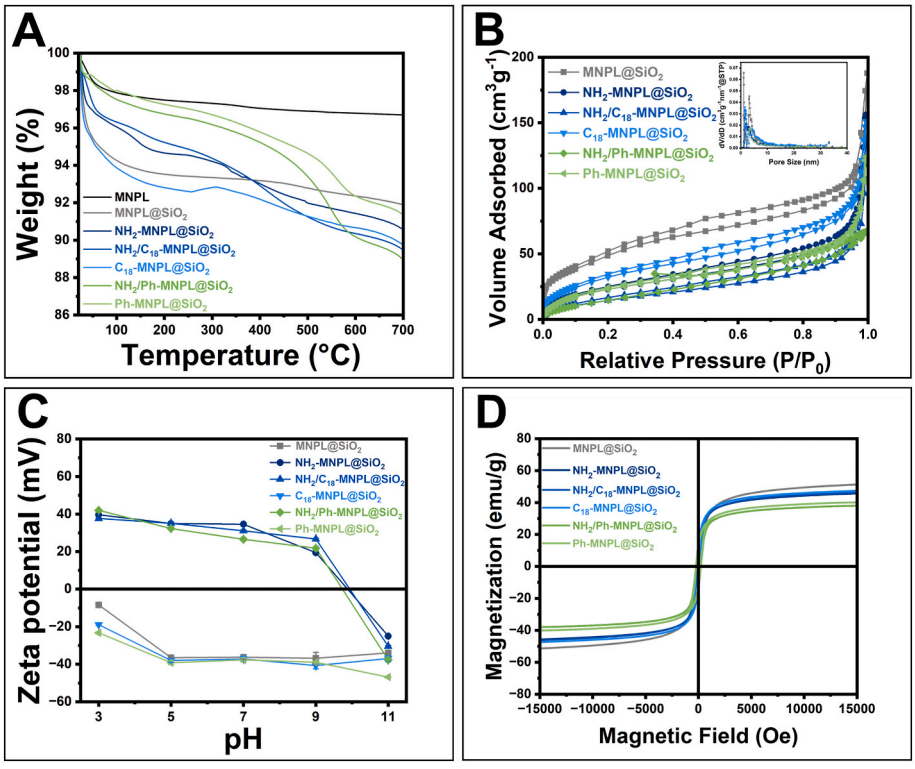

Fig. 3. (A) TGA, (B) N_2 sorption isotherms and pore size distributions (inset), (C) pH-dependent zeta (ζ) potentials, and (D) magnetic hysteresis (M–H) measurements of MNPL@SiO_2, NH_2-MNPL@SiO_2, NH_2/C_{18}-MNPL@SiO_2, C_{18}-MNPL@SiO_2, NH_2/Ph-MNPL@SiO_2, and Ph-MNPL@SiO_2.

(11.4–14.2 emu·g^{-1}) and H_c (104.0–229.9 Oe), suggesting soft ferrimagnetic behaviors (Rincon-Iglesias et al., 2022). Table S5 lists the M_s, which is the maximum magnetization they can achieve under an external magnetic field. The M_s of bare MNPL@SiO_2 was determined to be 51.1 emu·g^{-1}. The M_s values of functionalized MNPL@SiO_2 were comparable to or slightly lower than the 51.1 emu·g^{-1} obtained for bare MNPL@SiO_2, suggesting that the functionalization of MNPL@SiO_2 did not affect their unique physicochemical and magnetic properties.

3.2. Applications of functionalized MNPL@SiO_2 for magnetic field-assisted MNPs removal processes

3.2.1. Effects of the shape anisotropy of magnetic nanoparticles on the MNPs removal efficiency

Functionalized MNPL@SiO_2 was used to capture and remove MNPs from aqueous solutions under an external magnetic field using a permanent neodymium magnet. The processes involved the formation of MNPs-functionalized MNPL@SiO_2 complexes in suspension, where MNPs interact and adsorb onto functionalized MNPL@SiO_2, followed by the aggregation and migration of the complexes toward the magnet. After magnetic separation, the resulting composite was collected from the solution to remove MNPs. Fig. 4A presents the REs of MNPs using bare and functionalized MNPL@SiO_2. The RE of 100 nm diameter PS MNPs using plate-like MNPL (mean LS: 493.8 ± 107.5 nm; mean TN: 6.8 ± 1.7 nm) under an external magnetic field was 35.4 %, which is significantly higher than 1.7 % achieved using sphere-like Fe_3O_4 nanoparticles (mean diameter: 144.5 ± 23.8 nm) ($P < 0.001$) (Fig. 4A). Studies have shown that MNPs removal using spherical Fe_3O_4 nanoparticles involves surface adsorption as the primary mechanism, with the REs governed by the specific interactions at the nanoparticle interface (Wang et al., 2023). Considering the comparable M_s (78.5 and 65.4 emu·g^{-1}), zeta potentials (−0.0 ± 1.1 and −0.8 ± 0.2 mV), and S_{BET} (38.5 and 35.3 m^2 g^{-1}) of plate-like MNPL and spherical Fe_3O_4 nanoparticles, the differences in REs are likely due to the anisotropic plate-like morphologies of MNPL (Fig. S8 and Table S6).

3.2.2. Effects of the surface functionalization of MNPL@SiO_2 on MNPs removal efficiency

Fig. 5D–F shows the REs of MNPs using functionalized MNPL@SiO_2 as a function of the functional groups derivatized on the surface of MNPL@SiO_2 and the sizes of MNPs with the MNPL@SiO_2 dosage of 500 mg/L at pH = 7. A few aspects of the removal process are worth addressing. First, the REs of 100–1000 nm diameter PS MNPs using MNPL@SiO_2 functionalized with aminopropyl groups, such as NH_2-MNPL@SiO_2 and NH_2/C_{18}-MNPL@SiO_2 increased from 35.4 to ~95.5 % at 10 min of incubation. These results suggest that the increased REs can be attributed to the enhanced interactions between MNPs and magnetized aminopropyl functionalized MNPL@SiO_2 under an external magnetic field. Considering the measured zeta potentials (−20 to −80 mV) of MNPs, their surface is likely to be negatively charged in the pH range of 3–11 (Fig. S9). At pH = 7, the zeta potentials of NH_2-MNPL@SiO_2 and NH_2/C_{18}-MNPL@SiO_2 were +34.6 ± 0.8 and +31.1 ± 0.5 mV, respectively. These results suggest that electrostatic interactions between negatively charged MNPs and positively charged NH_2-MNPL@SiO_2 and NH_2/C_{18}-MNPL@SiO_2 play a key role in enhancing adsorption and achieving >~95 % RE. These trends were consistent across all sizes of MNPs. Second, the REs of octadecyl and phenylethyl functionalized MNPL@SiO_2, i.e., C_{18}-MNPL@SiO_2 and Ph-MNPL@SiO_2, were minimal (<~3 %) unless aminopropyl groups were co-functionalized alongside octadecyl and phenylethyl groups. These findings suggest that electrostatic interactions are more dominant than hydrophobic or π–π interactions in facilitating the adsorption of MNPs. Third, the REs of NH_2/Ph-MNPL@SiO_2 at pH = 7 increased from approximately 29.3 to 66.5 % as the size of the MNPs increased from 100 to 1000 nm, suggesting that incorporating phenylethyl groups to NH_2-MNPL@SiO_2 enhances RE, likely because the highly hydrophobic phenylethyl groups reinforce

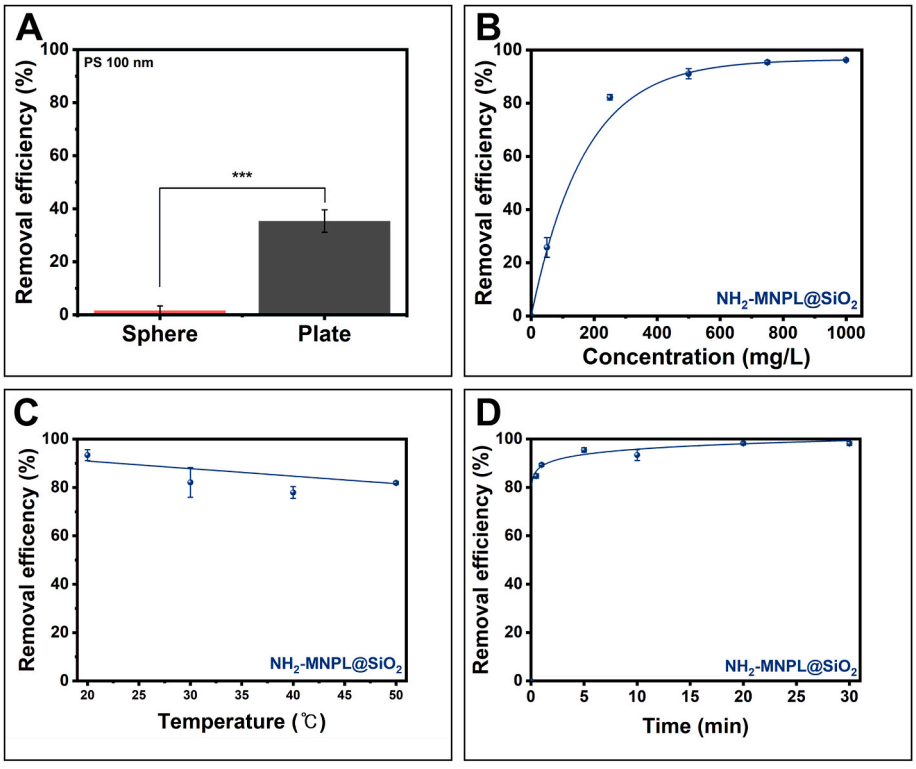

Fig. 4. MNPs removal efficiencies (REs), expressed as percentages of the amount of MNPs removed from the aqueous environments. (A) Comparison of (left) spherical Fe_3O_4 nanoparticles and (right) plate-like MNPLs used for removing 100 nm PS MNPs. RE of NH_2-MNPL@SiO_2 for removing 100 nm diameter PS MNPs as a function of (B) dosage, (C) temperature, and (D) time during the removal process. The error bars indicate the standard deviations of three independent experiments, and the asterisks show the significances of the differences (*, $P > 0.050$, **, $P < 0.005$; ***, $P < 0.001$).

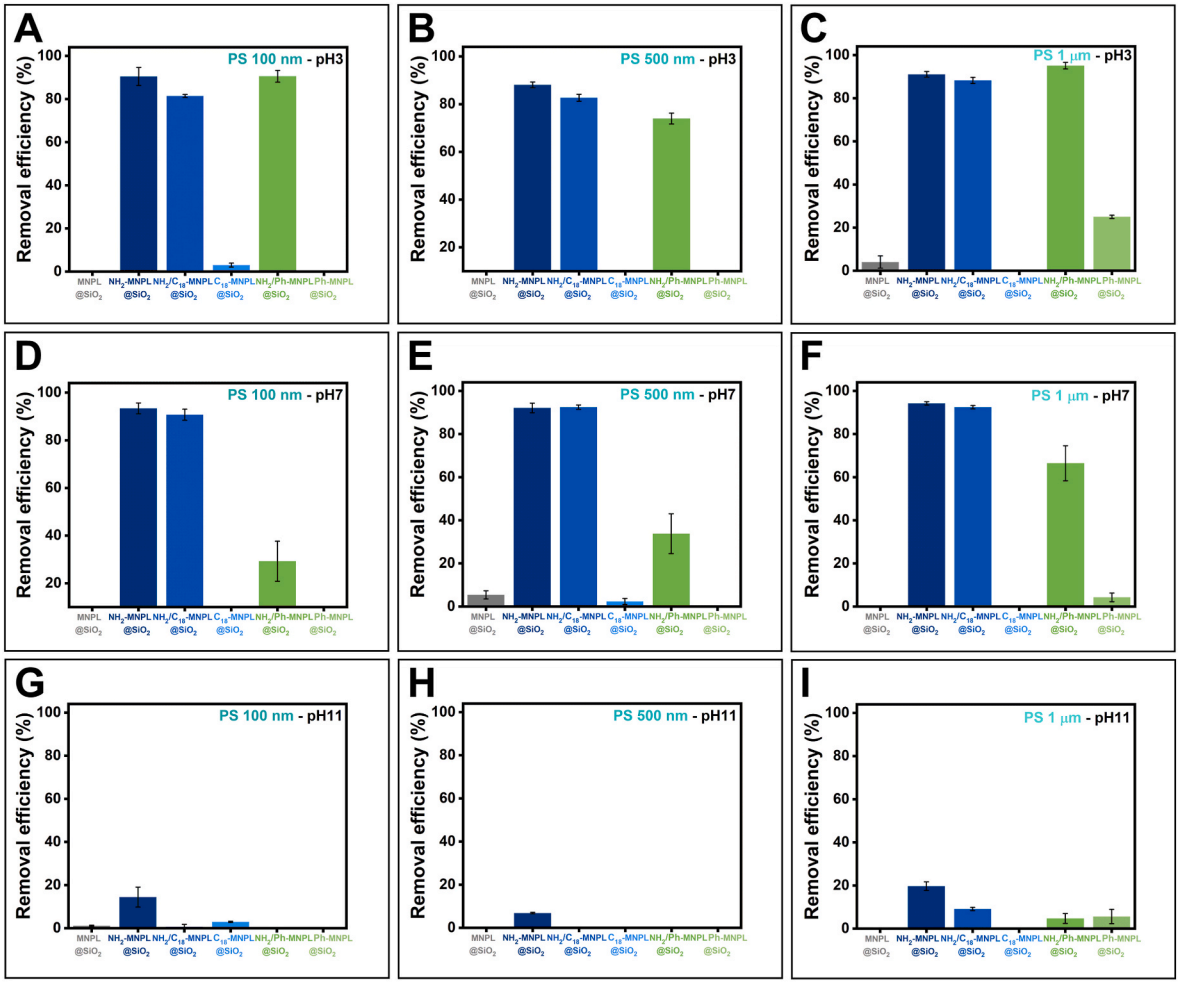

Fig. 5. MNPs REs of functionalized MNPL@SiO_2. Comparison of bare MNPL@SiO_2, NH_2-MNPL@SiO_2, mixed NH_2/C_{18}-MNPL@SiO_2, C_{18}-MNPL@SiO_2, mixed NH_2/Ph-MNPL@SiO_2, and Ph-MNPL@SiO_2 for removing (A) 100 nm, (B) 500 nm, (C) 1 μm diameter PS MNPs at pH 3; (D) 100 nm, (E) 500 nm, (F) 1 μm diameter PS MNPs at pH 7; and (G) 100 nm, (H) 500 nm, (I) 1 μm diameter PS MNPs at pH 11, respectively. The error bars represent the standard deviations of three independent experiments.

electrostatic interactions with hydrophobic or π–π interactions (or both) at larger MNPs sizes. In addition, comparing the REs of NH_2/C_{18}-MNPL@SiO_2 and NH_2/Ph-MNPL@SiO_2 shows that the effects of phenylethyl groups (contact angle: 85.6°) at pH = 3 are greater than those of octadecyl chains (contact angle: 32.5°) at pH = 7. This finding indicates that contact angle measurements (Fig. S7), which reflect bulk surface hydrophobicity, may not be sufficient to identify the dominant interactions at electrostatically complex nanoscale interfaces.

3.2.3. *Effects of the dosage, pH, and temperature on the MNPs removal efficiency*

Fig. 5 shows the effects of pH on 100–1000 nm diameter MNPs using functionalized MNPL@SiO_2. At pH = 3, all MNPLs@SiO_2 functionalized with aminopropyl groups, such as NH_2-MNPL@SiO_2, NH_2/C_{18}-MNPL@SiO_2, and NH_2/Ph-MNPL@SiO_2 exhibited REs higher than ~75 %, likely due to the complete protonation of NH_2– to NH_3^+–groups, maximizing the electrostatic attractions with negatively charged PS MNPs. Only NH_2/Ph-MNPL@SiO_2, exhibited a pH-dependent decline in RE as the pH was increased from 3 to 7, with the extent of the reduction varying according to the size of the MNPs. Hence, the π–π interactions or surface properties unique to phenylethyl groups may be sensitive to pH and the size of the MNPs. In contrast, the REs of all functionalized MNPL@SiO_2 dropped below ~10 % at pH = 11. These results suggest that electrostatic attractions between the protonated aminopropyl groups of functionalized MNPL@SiO_2 and negatively charged MNPs are the dominant removal mechanism at pH equal to or lower than 7. In addition, they suggest the deprotonation of aminopropyl groups weakens the electrostatic attraction, reducing the REs at pH > 7.

Fig. 4B and C shows the effects of functionalized MNPL@SiO_2 dosage and incubation temperature on the REs of 100 nm diameter MNPs using NH_2-MNPL@SiO_2. The REs of MNPs increased gradually as the concentration increased before saturation at NH_2-MNPL@SiO_2 concentrations >~800 mg/L. It was used for the remaining experiments, considering that a 500 mg/L dosage yielded REs of ~93.4 %. In addition, the REs remained above ~82 % across the temperature range of 20–50 °C, suggesting that thermally activated desorption was not significant enough to interfere with the removal processes.

3.2.4. *Magnetic field-assisted MNPs removal kinetics of functionalized MNPL@SiO_2*

Fig. 4D and S10 present the MNPs removal kinetics of NH_2-MNPL@SiO_2. Fig. 4 shows that more than 80 % of 100 nm diameter MNPs were removed rapidly using NH_2-MNPL@SiO_2 by electrostatic adsorption during the first 0.5 min of the experiments, and equilibrium was established as the RE reached ~95.5 % within 5 min. The results of NH_2-MNPL@SiO_2 were analyzed by obtaining the best fit to the data using a linearized form of the pseudo-first-order model, for which ln (q_e–q_t) was plotted as a function of t, and of the pseudo-second-order model, for which q_t/t was plotted versus t/q_e, where q_e and q_t is the equilibrium adsorption capacity and adsorption capacity measured at

time t, respectively. The reliability of each model was assessed by comparing its corresponding R-squared values (R^2). The inset plots in Fig. S10 and Table S7 show that the non-linearized and linearized forms of the pseudo-second-order model fit the data, resulting in a much higher correlation coefficient ($R^2 \approx 1$) than that of the pseudo-first-order model ($R^2 = 0.79$). The non-linear model appears to fit the data better at the earlier stage (Fig. S11), while the later stage follows a linearized model. Overall, a reasonable agreement between the experimental ($q_{e,exp}$) and calculated ($q_{e,fit}$) values further supports the validity of the pseudo-second-order model.

3.2.5. *Magnetic field-assisted MNPs removal isotherm of functionalized MNPL@SiO$_2$*

Fig. S12 shows the adsorption isotherm curves of NH_2-MNPL@SiO_2 for MNPs with diameters of 100 nm, 500 nm, and 1 μm, showing the relationship between the equilibrium adsorption capacity (q_e) and the equilibrium concentration (C_e) of MNPs at 25 °C and pH = 7.0. The adsorption behaviors of NH_2-MNPL@SiO_2 toward MNPs of 100 nm, 500 nm, and 1 μm diameter were analyzed by fitting the isotherm data to the Langmuir, Freundlich, and Temkin models. Fig. S13 presents the best fits to the equilibrium isotherms using the linearized forms of these models. Table S8 lists the isotherm parameters and correlation coefficients, such as R^2, obtained from these best fits. Based on the R^2 values, the Langmuir model provided a reasonably good fit to the adsorption data for MNPs, 100 nm, 500 nm, and 1 μm in diameter, using NH_2-MNPL@SiO_2. The estimated saturation adsorption capacities (q_m) of NH_2-MNPL@SiO_2 were 364.8, 1823.9, and 3630.2 $m^2\ g^{-1}$ for each size, respectively (Table S8). These values exceeded 99.8 $m^2\ g^{-1}$ of Fe-modified fly ash for 80 nm PS particles (Zhao et al., 2022), 319.5 $m^2\ g^{-1}$ of Cr-based MOF MIL-101 MOF for 50–70 nm PS particles (Modak et al., 2023), 6.3 $m^2\ g^{-1}$ of granular activated carbon for 100 nm PS particles (Arenas et al., 2021), 44.9 $m^2\ g^{-1}$ of pyrolyzed biochar for <500 nm PS particles (Ganie et al., 2021), and 2799.2 $m^2\ g^{-1}$ of iron oxide nanoparticles for 1 μm PS particles (Heo et al., 2022). In addition, a dimensionless factor R_L, one of the characteristic parameters of the Langmuir isotherm, was estimated using the fitted Langmuir constant K_L related to the affinity of binding sites and the initial MNPs concentration C_0 (see Eq. S(1)). It provides insight into the favorability of the adsorption process, indicating whether it is unfavorable ($R_L > 1$), linear ($R_L = 1$), favorable ($0 < R_L < 1$), or irreversible ($R_L = 0$) adsorption (Jang et al., 2020). The R_L of NH_2-MNPL@SiO_2 for the MNPs of all sizes was between 0 and 1, suggesting that the adsorption is a favorable process (Table S9).

3.2.6. *Effects of a magnetic field on the MNPs removal efficiency*

Fig. 6 shows the effects of the external magnetic field on the REs of NH_2-MNPL@SiO_2 for 100 nm, 500 nm, and 1 μm diameter PS MNPs. The REs increased by 18.2 ± 2.3 %, 5.2 ± 2.4 %, and 7.2 ± 2.0 % when the external magnetic field was applied compared to the controls in the absence of the field. The observed enhancements in RE may result from dynamic trapping processes induced by the external magnetic field of a neodymium magnet (Fig. 7). Magnetic nanoplates align with the static or dynamic magnetic field owing to their relatively high magnetic anisotropy and saturation magnetization. This alignment results in the formation of chain-like, sheet-like, or cluster aggregates via magnetic dipole–dipole interactions. These structures self-organize dynamically in the aqueous medium, forming porous, cage-like hierarchical architectures. In addition, magnetic nanoplates generate local fluid flow and disturbances in the surrounding solution as they aggregate and migrate toward the magnet. Consequently, unadsorbed MNPs are entrained by the converging flow fields or confined within the voids of the magnetized NH_2-MNPL@SiO_2 aggregates. The physical confinement within the void volumes and the dynamic flow fields produced by magnetized NH_2-MNPL@SiO_2 aggregates—collectively termed *dynamic trapping*—effectively prevent unadsorbed MNPs from escaping via mechanical or hydrodynamic entrapment. Once the aggregates are magnetically collected, unadsorbed MNPs trapped within the interstitial voids, even if not adsorbed on the surface of NH_2-MNPL@SiO_2, are concurrently removed.

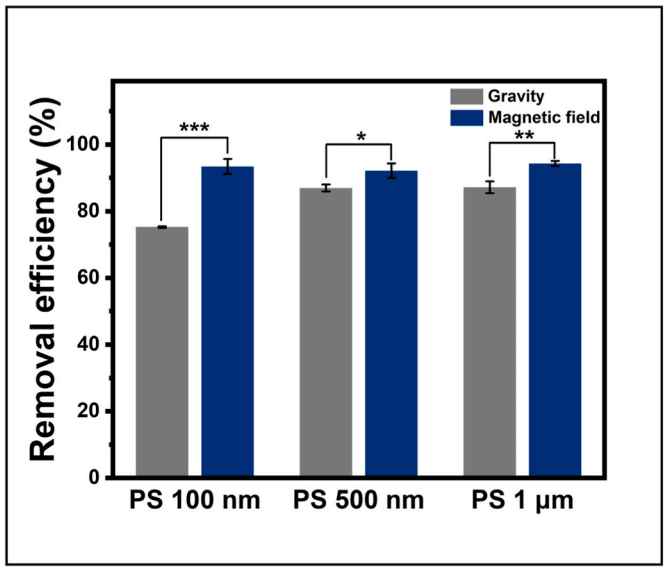

Fig. 6. Effects of an external magnetic field on the REs of NH_2-MNPL@SiO_2 for 100 nm, 500 nm, and 1 μm diameter PS MNPs. The error bars indicate the standard deviations of three independent experiments, and the asterisks show the significances of the differences (*, $P > 0.050$, **, $P < 0.005$; ***, $P < 0.001$).

A few experimental findings are consistent with the proposed hypothesis. First, the RE enhancement of unfunctionalized spherical Fe_3O_4 nanoparticles and plate-like MNPLs without SiO_2 coating in the presence of a magnetic field was less than 1 % and 5 % for 100 nm diameter MNPs, respectively. Notably, the RE of unfunctionalized MNPL@SiO_2, which has a negatively charged surface, in the presence of a magnetic field was less than 5 %, which is lower than the RE enhancement of the controls achieved by NH_2-MNPL@SiO_2 for 100 nm diameter MNPs. These results suggest that dynamic trapping is likely affected by the morphological differences between isotropic (i.e., spherical) and anisotropic (i.e., plate-like) nanostructures, which dictate the packing of their disordered aggregates. In addition, they suggest that dynamic trapping alone without specific surface interactions may be insufficient to account for the observed RE improvement. Second, the magnitude of the RE enhancements for NH_2-MNPL@SiO_2 depended on the MNPs' sizes compared to the controls in the absence of a magnetic field (Fig. 6). The RE of the controls without an external magnetic field was comparable to the maximum RE of NH_2-MNPL@SiO_2, as determined by the adsorption isotherms under saturation conditions. Third, under typical experimental conditions (50 mg/L MNPs and 500 mg/L magnetic nanoplate dosage), the additional amount of 100 nm diameter MNPs trapped was estimated to be approximately 24 % of the total MNPs removed via saturation adsorption. Assuming that the MNPs concentration (50 mg/L) remains constant over the 0–30 min removal process, the volume fraction containing additionally trapped 100 nm, 500 nm, and 1 μm diameter MNPs corresponds to approximately 43, 23, and 15 % of the total volume of 50 mg/L MNPs solution used for the removal experiments (Table S10). Fig. S14 and Table S11 show the packing fractions calculated from models of magnetic nanoplate aggregation with various geometric aspect ratios. The packing fraction of NH_2-MNPL@SiO_2 (LS: ~300 nm; TN: ~25 nm; aspect ratio: ~12) was estimated to be no greater than ~45 %, which would be even lower if other parameters, such as the LS and TN distributions of NH_2-MNPL@SiO_2, were considered. These results suggest that the aggregates have substantial void volumes due to structural disorder within the hierarchical assembly formed under magnetic field-assisted conditions. Consequently, the magnetic field-assisted aggregation of NH_2-MNPL@SiO_2 can significantly increase the amount of captured MNPs within void

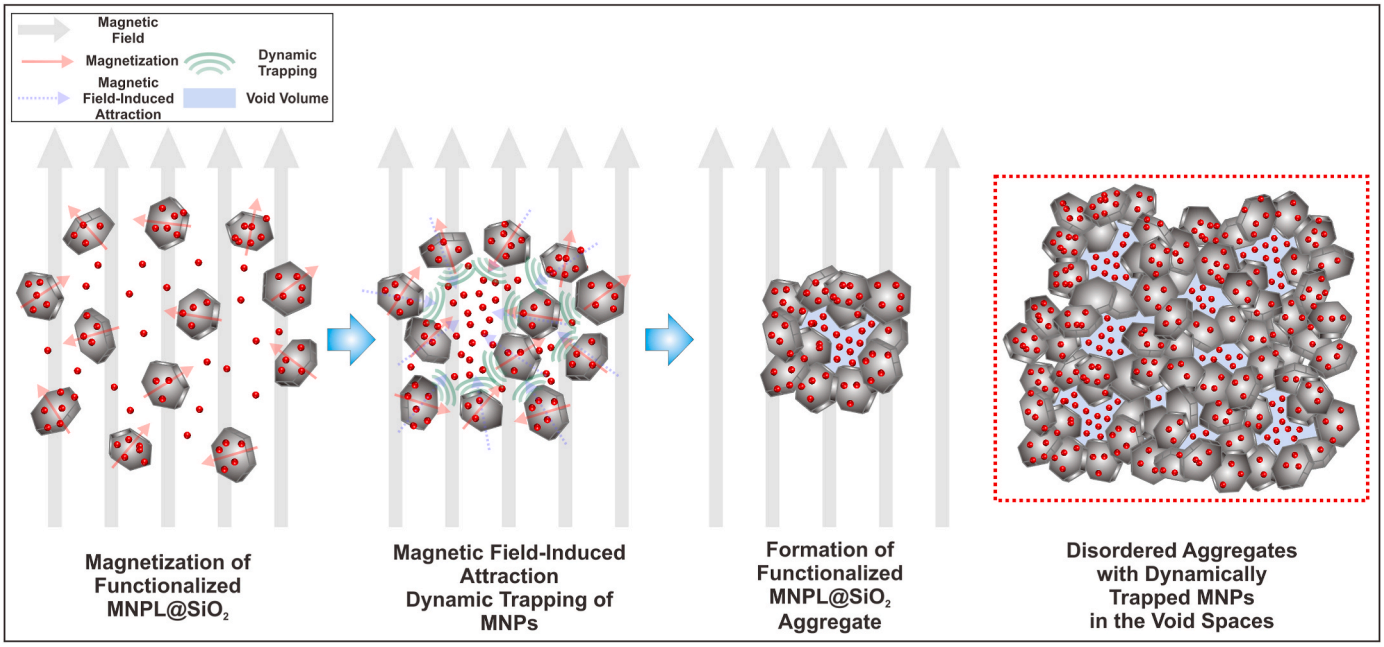

Fig. 7. Schematic illustration of the dynamic trapping process as a potential mechanism for RE enhancement in magnetic field-assisted MNPs removal.

volumes by dynamically entrapping unadsorbed MNPs, thereby contributing to the RE enhancements under magnetic field conditions. Lastly, the RE enhancement observed for 500 nm and 1 μm diameter MNPs was less than 50 % of that observed for 100 nm diameter MNPs, possibly because the larger MNPs were sterically more hindered and therefore less likely to be dynamically trapped or confined within the void structures of the aggregates than the smaller ones. Overall, higher observed REs than those predicted by electrostatic adsorption alone as the primary removal mechanism suggest that dynamic trapping plays an important secondary role in the MNPs removal process.

3.2.7. *Recovery and recycling of functionalized MNPL@SiO$_2$*

A series of experiments was conducted to assess the recovery and recycling potential of functionalized MNPL@SiO_2. As shown in Fig. S15, the cleaning efficiency of NH_2-MNPL@SiO_2 to remove 100 nm MNPs was evaluated along with the corresponding SEM images. Among the solvents tested, acetone showed the highest cleaning efficiency at ~85 %. The recycling feasibility was further investigated by measuring the REs over three cycles of the removal process. The REs decreased by no more than ~5 % during the first two cycles, as shown in Fig. S16. On the other hand, they decreased to ~45 % after the third cycle. FT-IR analysis on the NH_2-MNPL@SiO_2 adsorbents after multiple cycles confirmed that the core of the NH_2-MNPL@SiO_2 adsorbents and the functionalized surface remain intact, without any structural disruption or leaching of the grafted functional groups (Fig. S17). Therefore, the decrease in RE after the third cycle was attributed to incomplete regeneration (i.e., ~85 % cleaning efficiency) rather than structural deterioration. Nevertheless, these results suggest that while functionalized MNPL@SiO_2 holds considerable promise and potential for reuse, there is still room for further improvement.

4. Conclusions

Magnetic field-assisted removal experiments showed that the anisotropic shape of the functionalized MNPL@SiO_2 plays a crucial role in enhancing REs. Compared to spherical Fe_3O_4 nanoparticles, plate-like functionalized MNPL@SiO_2 achieved significantly higher REs (i.e., 35.4 % vs. 1.7 %) for 100 nm diameter MNPs under identical conditions. This improvement was attributed primarily to its plate-like geometry, offering higher specific surface areas and directional anisotropy, leading to unique aggregation behavior with a characteristic interfacial contact area under a magnetic field.

Surface functionalization is a key factor affecting MNPs capture and removal processes. Aminopropyl functionalized MNPL@SiO_2, such as NH_2-MNPL@SiO_2 and NH_2/C_{18}-MNPL@SiO_2, achieved high REs (>95 %) across various MNPs sizes, due primarily to strong electrostatic attraction between the positively charged, protonated amine and negatively charged MNPs surfaces at neutral pH. In contrast, octadecyl- and phenylethyl-functionalized MNPL@SiO_2, such as C_{18}-MNPL@SiO_2 and Ph-MNPL@SiO_2, exhibited minimal REs (<3 %) when not co-functionalized with aminopropyl groups, indicating limited contributions from hydrophobic or π–π interactions under the tested removal conditions.

An analysis of the MNPs adsorption kinetics and isotherms provided insight into the removal mechanisms. The kinetic data showed a good fit to the pseudo-second-order model, particularly during the initial stage, indicating chemisorption via surface complexation driven by electrostatic interactions. The Langmuir model produced a best fit for the isotherm data with high saturation adsorption capacities (q_m) of up to 3630.2 $m^2\ g^{-1}$ for 1 μm diameter MNPs, surpassing other nanostructured adsorbents, such as Fe-modified fly ash and granular activated carbon (Table S12).

An important secondary removal mechanism was identified, called dynamic trapping, induced by magnetic field-mediated aggregation of functionalized MNPL@SiO_2. This process, unique to the magnetic anisotropy of the plate-like MNPL@SiO_2, involves forming hierarchical porous aggregates that can physically entrap additional unadsorbed MNPs within their interstitial voids, even when the adsorption sites are saturated. The experimental results and modeling showed that dynamic trapping accounted for a substantial fraction of the RE increases, especially for smaller MNPs (e.g., 18.2 ± 2.3 % RE enhancement for 100 nm MNPs). Lastly, the reusability of NH_2-MNPL@SiO_2 was assessed through repeated cycles of MNPs removal and solvent cleaning. The results suggest that functionalized MNPL@SiO_2 has promising potential for reuse.

These findings hold significance from both engineering and scientific perspectives. First, the enhanced RE of MNPs can be attributed to the shape anisotropy of MNPL. Unlike their surface area or magnetization properties, their anisotropic morphology promotes more effective interactions and aggregation with MNPs under an external magnetic field.

The synergy between the anisotropic morphology and tailored surface functionalization enables rapid, highly efficient, and size-tunable MNPs removal, achieving more than ~95 % RE for MNPs with sizes ranging from 100 to 1000 nm within 10 min. Second, the discovery of dynamic trapping, a magnetic field-driven physical confinement mechanism for capturing MNPs, introduces a previously unrecognized pathway for MNPs removal, offering a novel mechanistic insight into functional nanomaterial-assisted pollutant removal beyond classical adsorption models.

Scaling up functionalized MNPL@SiO_2-based MNPs removal processes from the laboratory to pilot or industrial operations faces multiple challenges. For example, producing large quantities of MNPL@SiO_2 adsorbents with controlled lateral size, thickness, and uniform crystalline magnetic domains passivated with a precise silica shell, along with robust surface functionalization steps, requires quality control to ensure batch-to-batch reproducibility and consistency. While magnetic separation performs very well in laboratory settings, maintaining high separation efficiency becomes more challenging when scaling up to larger volumes and higher flow rates. In addition, generating a strong, uniform magnetic field or gradient suitable for effective separation and recovery in a large-volume reactor is a nontrivial task that demands a sophisticated system design. Moreover, establishing reliable regeneration cycles for functionalized MNPL@SiO_2 adsorbents remains a barrier to ensuring their long-term reusability in large-scale industrial applications. These challenges are accompanied by economic feasibility that is contingent on time, cost, and environmental and safety constraints in real-world, continuous, high-throughput processes. Addressing these challenges, along with our findings, has important implications and can present new opportunities for developing rapid, efficient, and sustainable nanomaterials-based solutions for industrial effluent treatment, wastewater management, and broad natural water purification.

CRediT authorship contribution statement

Yujeong Jeong: Writing – original draft, Visualization, Resources, Methodology, Investigation, Formal analysis, Data curation. **Eun-Hye Jang:** Writing – original draft, Visualization, Resources, Methodology, Investigation, Formal analysis, Data curation. **Gaeun Kim:** Resources, Investigation. **Kyubeom Lee:** Resources, Investigation. **Joonkyung Jang:** Writing – original draft, Investigation, Data curation. **Sungwook Chung:** Writing – review & editing, Writing – original draft, Visualization, Validation, Supervision, Resources, Project administration, Methodology, Investigation, Funding acquisition, Formal analysis, Data curation, Conceptualization.

Declaration of competing interest

The authors declare that they have no known competing financial interests or personal relationships that could have appeared to influence the work reported in this paper.

Acknowledgments

This work was supported by Basic Science Research Program through the National Research Foundation of Korea (NRF) funded by the Ministry of Education (NRF-2022R1I1A1A01073371 and RS-2024-00412964), the Korean government (Ministry of Trade, Industry and Energy, Ministry of Science and ICT, Ministry of the Interior and Safety, National Fire Agency, Project Number: 1761002860) and 2023 BK21 FOUR Graduate School Innovation Support funded by Pusan National University (PNU-Fellowship program).

Appendix A. Supplementary data

Supplementary data to this article can be found online at https://doi.org/10.1016/j.jenvman.2025.128396.

Data availability

Data will be made available on request.

References

Abdelsamad, A.M., Saeidi, N., Mackenzie, K., 2025. Mesoporous silica nanoparticles for rapid removal of PFOA: impact of surface functional groups on adsorption efficiency and adsorbent regeneration. Environmental Pollution 383, 126796.
Ahmed, M.B., Rahman, M.S., Alom, J., Hasan, M.S., Johir, M., Mondal, M.I.H., Lee, D.-Y., Park, J., Zhou, J.L., Yoon, M.-H., 2021. Microplastic particles in the aquatic environment: a systematic review. Sci. Total Environ. 775, 145793.
Arenas, L.R., Gentile, S.R., Zimmermann, S., Stoll, S., 2021. Nanoplastics adsorption and removal efficiency by granular activated carbon used in drinking water treatment process. Sci. Total Environ. 791, 148175.
Asemani, M., Rabbani, A.R., 2020. Detailed FTIR spectroscopy characterization of crude oil extracted asphaltenes: curve resolve of overlapping bands. J. Petrol. Sci. Eng. 185, 106618.
Bai, X., Xiao, Y., Wu, K., Liu, T., Li, Z., 2025. As (III) removal from drinking water using FMCTO@ Fe_3O_4 in the adsorption-magnetic separation-sand filtration equipment: Trade-off between as removal efficiency and adsorbent utilization rate. Water Res. 277, 123308.
Chabi, K., Li, J., Ye, C., Kiki, C., Xiao, X., Li, X., Guo, L., Gad, M., Feng, M., Yu, X., 2024. Rapid sand filtration for< 10 μm-sized microplastic removal in tap water treatment: efficiency and adsorption mechanisms. Sci. Total Environ. 912, 169074.
Chen, C.-Y., Lin, Z., 2024. Exploring the potential and challenges of developing physiologically-based toxicokinetic models to support human health risk assessment of microplastic and nanoplastic particles. Environ. Int. 186, 108617.
Chen, G., Feng, Q., Wang, J., 2020. Mini-review of microplastics in the atmosphere and their risks to humans. Sci. Total Environ. 703, 135504.
Chen, H., Yang, X., Lin, M., Li, D., Wang, B., Shen, J., Long, J., Dai, W., Wang, X., Zhang, Z., 2023. Dual Z-scheme heterojunction SiC-sandwiched $InVO_4$ nanoflowers for boosting visible-light photocatalytic CO_2 reduction with H_2O. ACS Sustain. Chem. Eng. 11, 18029–18040.
Choi, Y.R., Kim, Y.-N., Yoon, J.-H., Dickinson, N., Kim, K.-H., 2021. Plastic contamination of forest, urban, and agricultural soils: a case study of yeoju city in the Republic of Korea. J. Soils Sediments 21, 1962–1973.
Cózar, A., Echevarría, F., González-Gordillo, J.I., Irigoien, X., Úbeda, B., Hernández-León, S., Palma, Á.T., Navarro, S., García-de-Lomas, J., Ruiz, A., 2014. Plastic debris in the open ocean. Proc. Natl. Acad. Sci. 111, 10239–10244.
Dayal, L., Yadav, K., Dey, U., Das, K., Kumari, P., Raj, D., Mandal, R.R., 2024. Recent advancement in microplastic removal process from wastewater-a critical review. J. Hazard. Mater. Adv. 16, 100460.
de Sousa, F.D.B., 2024. The global plastics treaty: understanding the present to guide the future. Cambridge Prisms: Plastics 2, e31.
Dong, C.-D., Chen, C.-W., Chen, Y.-C., Chen, H.-H., Lee, J.-S., Lin, C.-H., 2020. Polystyrene microplastic particles: in vitro pulmonary toxicity assessment. J. Hazard Mater. 385, 121575.
Du, R., Lin, H., Sun, J., Zhang, J., Luo, J., Huang, X., Pan, Z., 2024. Unveiling the suspended atmospheric microplastic pollution in a coastal urban landscape. J. Clean. Prod. 442, 141145.
Eerkes-Medrano, D., Thompson, R.C., Aldridge, D.C., 2015. Microplastics in freshwater systems: a review of the emerging threats, identification of knowledge gaps and prioritisation of research needs. Water Res. 75, 63–82.
Falco, G., Fenti, A., Galoppo, S., Chianese, S., Musmarra, D., Cocca, M., Mallardo, S., Iovino, P., 2024. Promoting removal of polystyrene microplastics from wastewater by electrochemical treatment. Journal of Water Process Engineering 68, 106418.
Fatmawati, T., Shiddiq, M., Armynah, B., Tahir, D., 2023. Synthesis methods of Fe_3O_4 nanoparticles for biomedical applications. Chem. Eng. Technol. 46, 2356–2366.
Fidelis, R.d.J.A., Pires, M., de Resende, D.S., Lima, G.F.C., de Paiva, P.R.P., da Silva Bezerra, A.C., 2025. Magnetite: properties and applications–A review. J. Magn. Magn Mater. 614, 172770.
Foo, K.Y., Hameed, B.H., 2010. Insights into the modeling of adsorption isotherm systems. Chemical engineering journal 156, 2–10.
Ganie, Z.A., Khandelwal, N., Tiwari, E., Singh, N., Darbha, G.K., 2021. Biochar-facilitated remediation of nanoplastic contaminated water: effect of pyrolysis temperature induced surface modifications. J. Hazard Mater. 417, 126096.
Heo, Y., Lee, E.-H., Lee, S.-W., 2022. Adsorptive removal of micron-sized polystyrene particles using magnetic iron oxide nanoparticles. Chemosphere 307, 135672.
Hoang, V.-H., Nguyen, M.-K., Hoang, T.-D., Ha, M.C., Huyen, N.T.T., Bui, V.K.H., Pham, M.-T., Nguyen, C.-M., Chang, S.W., Nguyen, D.D., 2024. Sources, environmental fate, and impacts of microplastic contamination in agricultural soils: a comprehensive review. Sci. Total Environ. 950, 175276.
Hu, J., Qin, X., Zhang, J., Zhu, Y., Zeng, W., Lin, Y., Liu, X., 2021. Polystyrene microplastics disturb maternal-fetal immune balance and cause reproductive toxicity in pregnant mice. Reprod. Toxicol. 106, 42–50.
Huang, L., Zeng, T., Xu, X., He, Z., Chen, J., Song, S., 2019. Immobilized hybrids between nitrogen-doped carbon and stainless steel derived Fe_3O_4 used as a heterogeneous activator of persulfate during the treatment of aqueous carbamazepine. Chem. Eng. J. 372, 862–872.
Huang, Z., Wu, K., Yu, Q.-H., Wang, Y.-Y., Xing, J., Xia, T.-L., 2016. Facile synthesis of size tunable Fe_3O_4 nanoparticles in bisolvent system. Chem. Phys. Lett. 664, 219–225.

Jang, E.-H., Pack, S.P., Kim, I., Chung, S., 2020. A systematic study of hexavalent chromium adsorption and removal from aqueous environments using chemically functionalized amorphous and mesoporous silica nanoparticles. Sci. Rep. 10, 5558.
Jeong, Y., Kim, B., Sathiyavahisan, L.P., Mahadi, R., Lee, K., Jang, E.-H., Choe, Y., Oh, Y.-K., Chung, S., 2023. Preparation of two-dimensional Fe_3O_4 nanodisks and nanosheets transformed from α-Fe_2O_3 analogues and their applications in magnetic field-assisted microalgal harvesting biorefinery processes. ACS Sustain. Chem. Eng. 12, 2018–2027.
Jeong, Y., Lee, K., Kim, G., Jang, E.-H., Choe, Y., Kim, S., Chung, S., 2025. Preparation of TiO_2/α-Fe_2O_3@SiO_2 nanorod heterostructures and their applications for efficient photodegradation of methylene blue. Crystals 15, 277.
Jin, H., Yang, C., Jiang, C., Li, L., Pan, M., Li, D., Han, X., Ding, J., 2022. Evaluation of neurotoxicity in BALB/c mice following chronic exposure to polystyrene microplastics. Environmental health perspectives 130, 107002.
Jing, N., Chen, C., Yuan, X., Ma, X., Teng, G., Zhang, J., Li, X., Wu, Z., 2025. Recyclable Fe_3O_4-decorated attapulgite nano-networks with alternating magnetic field response for continuous pest management and iron fertilizer application. Chem. Eng. J. 504, 158904.
Kang, T., Jang, I., Oh, S.-G., 2016. Surface modification of silica nanoparticles using phenyl trimethoxy silane and their dispersion stability in N-methyl-2-pyrrolidone. Colloids Surf. A Physicochem. Eng. Asp. 501, 24–31.
Kumari, S., Sharma, O.P., Gusain, R., Mungse, H.P., Kukrety, A., Kumar, N., Sugimura, H., Khatri, O.P., 2015. Alkyl-chain-grafted hexagonal boron nitride nanoplatelets as oil-dispersible additives for friction and wear reduction. ACS applied materials & interfaces 7, 3708–3716.
Li, C., Busquets, R., Campos, L.C., 2024. Enhancing microplastic removal from natural water using coagulant aids. Chemosphere 364, 143145.
Li, W., Wu, C., Xiong, Z., Liang, C., Li, Z., Liu, B., Cao, Q., Wang, J., Tang, J., Li, D., 2022. Self-driven magnetorobots for recyclable and scalable micro/nanoplastic removal from nonmarine waters. Sci. Adv. 8.
Li, Y., Gao, Y., Fan, B., Guan, L., Zhao, B., Zhang, R., 2021. Tailoring microwave electromagnetic responses in $Ti_3C_2T_x$ MXene with Fe_3O_4 nanoparticle decoration via a solvothermal method. J. Phys. Chem. C 125, 19914–19924.
Liang, Y., Lin, X., Liao, H., Hasan, M., Gong, S., Zhou, X., 2025. Nanocapsule decorated reduced graphene oxide/Schiff base functionalized Fe_3O_4 for effective detection of Cd (II) and anti-interference properties. Chem. Eng. J. 507, 160606.
Liu, H., Ji, S., Yang, H., Zhang, H., Tang, M., 2014. Ultrasonic-assisted ultra-rapid synthesis of monodisperse meso-SiO_2@ Fe_3O_4 microspheres with enhanced mesoporous structure. Ultrason. Sonochem. 21, 505–512.
Majoul, N., Aouida, S., Bessaïs, B., 2015. Progress of porous silicon APTES-functionalization by FTIR investigations. Appl. Surf. Sci. 331, 388–391.
Mao, Y., Hu, Z., Li, H., Zheng, H., Yang, S., Yu, W., Tang, B., Yang, H., He, R., Guo, W., 2024. Recent advances in microplastic removal from drinking water by coagulation: removal mechanisms and influencing factors. Environmental Pollution 349, 123863.
Mistral, J., Ve Koon, K.T., Fernando Cotica, L., Sanguino Dias, G., Aparecido Santos, I., Alcouffe, P., Milhau, N., Pin, D., Chapet, O., Serghei, A., 2024. Chitosan-coated superparamagnetic Fe_3O_4 nanoparticles for magnetic resonance imaging, magnetic hyperthermia, and drug delivery. ACS Appl. Nano Mater. 7, 7097–7110.
Mitra, A., Mohapatra, J., Aslam, M., 2024. Magnetic and electronic properties of anisotropic magnetite nanoparticles. Mater. Res. Express 11, 022002.
Modak, S., Kasula, M., Esfahani, M.R., 2023. Nanoplastics removal from water using metal–organic framework: investigation of adsorption mechanisms, kinetics, and effective environmental parameters. ACS Applied Engineering Materials 1, 744–755.
Nguyen, M.D., Tran, H.-V., Xu, S., Lee, T.R., 2021. Fe_3O_4 nanoparticles: structures, synthesis, magnetic properties, surface functionalization, and emerging applications. Applied Sciences 11, 11301.
Pan, Z., Wang, D., Zhang, D., Yang, Y., Yu, H., Wang, T., Dong, X., 2024. rGO doped MOFs derived α-Fe_2O_3 nanomaterials for self-supporting ppb-level NO_2 gas sensor. Sensor. Actuator. B Chem. 405, 135378.
Patidar, K., Ambade, B., Mohammad, F., Soleiman, A.A., 2023a. Microplastics as heavy metal vectors in the freshwater environment: distribution, variations, sources and health risk. Phys. Chem. Earth, Parts A/B/C 131, 103448.
Patidar, K., Ambade, B., Verma, S.K., Mohammad, F., 2023b. Microplastic contamination in water and sediments of mahanadi river, India: an assessment of ecological risk along rural-urban area. J. Environ. Manag. 348, 119363.
Patidar, K., Ambade, B., Younis, A.M., Alluhayb, A.H., 2024. Characteristics, fate, and sources of microplastics contaminant in surface water and sediments of river water. Phys. Chem. Earth, Parts A/B/C 134, 103596.
Pedrero, D., Edo, C., Fernández-Piñas, F., Rosal, R., Aguado, S., 2024. Efficient removal of nanoplastics from water using mesoporous metal organic frameworks. Separation and Purification Technology 333, 125816.
Perumpully, S.J., Kumar, R.P., Gautam, S., Ambade, B., Gautam, A.S., 2023. An inclusive trend study of evaluation and scientometric analysis of microplastics. Phys. Chem. Earth, Parts A/B/C 132, 103455.
Pervaiz, S., Javed, M., Shah, A., Latif, A., Nasir, S., Shah, I., 2025. Environmental applications of magnetic nanohybrid materials. RSC advances 15, 19899–19936.
Phouthavong, V., Yan, R., Nijpanich, S., Hagio, T., Ichino, R., Kong, L., Li, L., 2022. Magnetic adsorbents for wastewater treatment: advancements in their synthesis methods. Materials 15, 1053.
Rincon-Iglesias, M., Rodrigo, I.B., Berganza, L., Serea, E.S.A., Plazaola, F., Lanceros-Mendez, S., Lizundia, E., Reguera, J., 2022. Core–shell Fe_3O_4@Au nanorod-loaded gels for tunable and anisotropic magneto-and photothermia. ACS Appl. Mater. Interfaces 14, 7130–7140.
Salman, A.D., Juzsakova, T., Ákos, R., Ibrahim, R.I., Al-Mayyahi, M.A., Mohsen, S., Abdullah, T.A., Domokos, E., 2021. Synthesis and surface modification of magnetic Fe_3O_4@SiO_2 core-shell nanoparticles and its application in uptake of scandium (III) ions from aqueous media. Environ. Sci. Pollut. Control Ser. 28, 28428–28443.
Sankar, T.K., Kumar, A., Mahto, D.K., Das, K.C., Narayan, P., Fukate, M., Awachat, P., Padghan, D., Mohammad, F., Al-Lohedan, H.A., 2023. The health risk and source assessment of polycyclic aromatic hydrocarbons (PAHs) in the soil of industrial cities in India. Toxics 11, 515.
Seo, J.Y., Praveenkumar, R., Kim, B., Seo, J.-C., Park, J.-Y., Na, J.-G., Jeon, S.G., Park, S. B., Lee, K., Oh, Y.-K., 2016. Downstream integration of microalgae harvesting and cell disruption by means of cationic surfactant-decorated Fe_3O_4 nanoparticles. Green Chem. 18, 3981–3989.
Shi, B., Xie, L., Ma, B., Zhou, Z., Xu, B., Qu, L., 2022. Preparation and properties of highly transparent SiO_2 aerogels for thermal insulation. Gels 8, 744.
Sing, K.S., 1985. Reporting physisorption data for gas/solid systems with special reference to the determination of surface area and porosity (recommendations 1984). Pure Appl. Chem. 57, 603–619.
Sumathi, Y., Kumar, P., Singhania, R.R., Chen, C.-W., Gurunathan, B., Dong, C.-D., Patel, A.K., 2025. Harnessing Fe_3O_4 nanoparticles for sustainable harvesting of astaxanthin-producing microalgae: advancing industrial-scale biorefinery. Separation and Purification Technology 353, 128408.
Sun, J., Peng, Z., Zhu, Z.-R., Fu, W., Dai, X., Ni, B.-J., 2022. The atmospheric microplastics deposition contributes to microplastic pollution in urban waters. Water Res. 225, 119116.
Thommes, M., Kaneko, K., Neimark, A.V., Olivier, J.P., Rodriguez-Reinoso, F., Rouquerol, J., Sing, K.S., 2015. Physisorption of gases, with special reference to the evaluation of surface area and pore size distribution (IUPAC technical report). Pure Appl. Chem. 87, 1051–1069.
Tomić, M., Fohlerova, Z., Gràcia, I., Figueras, E., Cané, C., Vallejos, S., 2021. UV-light activated APTES modified WO_{3-x} nanowires sensitive to ethanol and nitrogen dioxide. Sensor. Actuator. B Chem. 328, 129046.
Wang, H.-P., Huang, X.-H., Chen, J.-N., Dong, M., Nie, C.-Z., Qin, L., 2023. Modified superhydrophobic magnetic Fe_3O_4 nanoparticles for removal of microplastics in liquid foods. Chem. Eng. J. 476, 146562.
Yoon, S.-Y., Lee, C.-G., Park, J.-A., Kim, J.-H., Kim, S.-B., Lee, S.-H., Choi, J.-W., 2014. Kinetic, equilibrium and thermodynamic studies for phosphate adsorption to magnetic iron oxide nanoparticles. Chemical engineering journal 236, 341–347.
Zhao, H., Huang, X., Wang, L., Zhao, X., Yan, F., Yang, Y., Li, G., Gao, P., Ji, P., 2022. Removal of polystyrene nanoplastics from aqueous solutions using a novel magnetic material: adsorbability, mechanism, and reusability. Chem. Eng. J. 430, 133122.